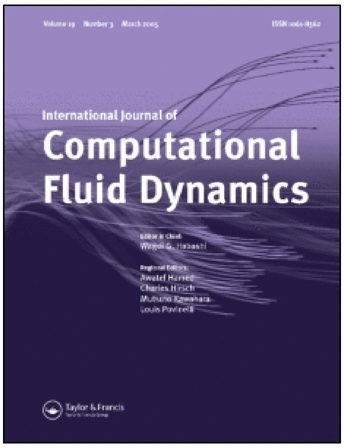

International Journal of Computational Fluid Dynamics
Publication details, including instructions for authors and subscription information:
http://www.informaworld.com/smpp/title~content=t713455064

Shock-unsteadiness model applied to oblique shock wave/turbulent boundary-layer interaction

Amjad Ali Pasha [a]; Krishnendu Sinha [a]
[a] Department of Aerospace Engineering, Indian Institute of Technology Bombay, Mumbai, India

Online Publication Date: 01 September 2008

To cite this Article Ali Pasha, Amjad and Sinha, Krishnendu(2008)'Shock-unsteadiness model applied to oblique shock wave/turbulent boundary-layer interaction',International Journal of Computational Fluid Dynamics,22:8,569 — 582

To link to this Article: DOI: 10.1080/10618560802290284

URL: http://dx.doi.org/10.1080/10618560802290284

International Journal of Computational Fluid Dynamics
Vol. 22, No. 8, September 2008, 569–582

Shock-unsteadiness model applied to oblique shock wave/turbulent boundary-layer interaction

Amjad Ali Pasha and Krishnendu Sinha*

Department of Aerospace Engineering, Indian Institute of Technology Bombay, Mumbai, India

(*Received 26 December 2007; final version received 12 June 2008*)

Reynolds-averaged Navier–Stokes prediction of shock wave/turbulent boundary layer interactions can yield significant error in terms of the size of the separation bubble. In many applications, this can alter the shock structure and the resulting surface properties. Shock-unsteadiness modification of Sinha *et al*. (Physics of Fluids, Vol.15, No.8, 2003) has shown potential in improving separation bubble prediction in compression corner flows. In this article, the modification is applied to oblique shock wave interacting with a turbulent boundary layer. The challenges involved in the implementation of the shock-unsteadiness correction in the presence of multiple shock waves and expansion fans are addressed in detail. The results show that a robust implementation of the model yields appreciable improvement over standard k–ω turbulence model predictions.

Keywords: high-speed flows; turbulent boundary layer; shock-unsteadiness; separation bubble; turbulence modelling

Nomenclature

b_1'	shock-unsteadiness damping parameter
C_f	skin friction coefficient
k	turbulent kinetic energy
M_{1n}	upstream Mach number normal to shock
P_k	production of turbulent kinetic energy
S_{ij}	mean strain rate tensor
S_{ii}	mean dilatation
β	shock generator deflection angle
μ_T	eddy viscosity
μ	molecular viscosity
ω	turbulent specific dissipation rate

Subscripts

0	upstream of interaction
w	wall condition
∞	freestream conditions

1. Introduction

Practically, many flows are turbulent in nature. In high-speed flows, shock waves interact with the turbulent boundary layer, altering its characteristics and thereby changing surface properties like pressure, skin friction and heat transfer. Some examples of such interactions are in compression corner, oblique shock impingement on a surface, single fin and double fin configurations. In a hypersonic vehicle, shock wave from the nose can interact with the turbulent boundary layer in the inlet of scramjet engines. Such oblique shock wave/turbulent boundary layer interaction can significantly affect the flow in the engine inlet and degrade its performance. Accurate flow prediction in these interaction regions is therefore important for the design and operation of scramjet engines. When a shock wave interacts with a boundary layer, the strong adverse pressure across the shock can cause the boundary layer to separate. The location and size of the separation bubble has a strong influence on the flow pattern as well as pressure and heat transfer. Pressure increases at separation point, and increases further at reattachment. Heat transfer rate and skin friction attain high values at reattachment point. Flow separation and reattachment often generate additional shock waves and expansion fans which interact among them to result in a complex flow pattern.

Reynolds-averaged Navier–Stokes (RANS) equations are often used to compute shock wave/turbulent boundary layer interaction. Compared with experimental data, conventional two-equation turbulence models generally result in later separation of the boundary layer (Viegas and Horstman 1979, Coakley and Huang 1992, Lindbad *et al*. 1998). They also

*Corresponding author. Email: krish@aero.iitb.ac.in

ISSN 1061-8562 print/ISSN 1029-0257 online

DOI: 10.1080/10618560802290284
http://www.informaworld.com

underpredict separation bubble size and overpredict the heat transfer rate at reattachment point. These limitations in RANS computations are often attributed to the fact that the turbulence models do not account for the unsteady nature of these interactions. In a pioneering study, Sinha *et al.* (2003) found that unsteady shock interaction with incoming turbulence fluctuations dampens the amplification of turbulent kinetic energy. A correction was added to standard two-equation turbulence models to account for this damping effect. The resulting model was found to match DNS data of turbulent kinetic energy amplification across a shock. The shock unsteadiness modification when applied to supersonic flow over compression corner geometry improved the prediction of separation shock location and the resulting pressure distribution (Sinha *et al.* 2005).

In this article, we apply the shock unsteadiness correction to the interaction of an oblique shock wave with a turbulent boundary layer. Presence of multiple shock waves and flow expansion in the interaction region make it more challenging to implement the shock-unsteadiness correction than earlier compression corner applications. The function used to identify the location and the extent of shock waves needs to be altered. Also, the variation of flow quantities upstream of the different shock waves cannot be prescribed *a priori*, as in the compression corner cases. This article addresses these issues in detail and presents an improved implementation of the shock-unsteadiness modification for practical flows.

This article is organised as follows. The next section describes the geometry and flow conditions for the test case of Schulein (2006) experiments. Next, we present a summary of governing equations and shock-unsteadiness modification to the k–ω model followed by the numerical method and boundary conditions applied in the simulations. The last section compares the computed results using standard and shock-unsteadiness modified k–ω turbulence models with experimental data.

2. Test case

Experiments were performed by Schulein (2006) for oblique shock wave/turbulent boundary layer interaction flows. The geometry, shown schematically in Figure 1a, consists of a flat plate and a shock generator with three different deflection angles of 6, 10 and 14°. The strength of the incident shock wave increases with deflection angle, resulting in a stronger interaction with the boundary layer. The inviscid shock from tip of shock generator interacts with the turbulent boundary layer developed over the flat plate. Free stream conditions are $M_\infty = 5$, $T_\infty = 68.3$ K and $p_\infty = 4008.5$ N/m^2 with unit Reynolds number $Re_\infty = 37 \times 10^6\,\mathrm{m}^{-1}$. The plate is maintained under isothermal conditions of 300 K. Initially, the experiments were done for flow over flat plate to obtain undisturbed turbulent boundary layer properties like δ, δ^*, θ and C_f at different locations. Wall data like pressure, skin friction and heat transfer rates were measured along the flat plate in the interaction region.

3. Simulation methodology

We solve the two-dimensional Favre-averaged Navier–Stokes equations presented by Wilcox (1998) for the mean flow. The two-equation k–ω model of Wilcox (1988) and the recent shock-unsteadiness corrected k–ω model of Sinha *et al.* (2005) are used in the simulations. Both the standard and shock-unsteadiness corrected k–ω models do not include any compressibility corrections. The governing equations are discretised in a finite volume formulation where the inviscid fluxes are computed using a modified, low-dissipation form of the Steger–Warming flux splitting approach (MacCormack and Candler 1989). The turbulence model equations are fully coupled to the mean flow equations. The details of the formulation are given by Sinha and Candler (1998). The method is second-order accurate in stream-wise and wall normal directions. The viscous fluxes and the turbulent source terms are evaluated using second-order accurate central difference method. The implicit Data Parallel Line Relaxation method of Wright *et al.* (1998) is used to integrate in time and reach steady-state solution.

The computational domain is schematically shown in Figure 1b. It extends 85 mm upstream and 150 mm downstream of the interaction region in the wall parallel direction. In the wall normal direction, it extends to 44 mm such that the top boundary is above the oblique shock entry and exit locations. The experiments (Schulein 2006) were done over a 500-mm long flat plate, and the inviscid shock was adjusted to impinge at a fixed location of 350 mm from the tip of shock generator. Inviscid simulations were done to locate the shock impingement point. This point is taken as origin in the computational domain such that negative values of x are assigned upstream and positive values in the downstream side. The inviscid shock impingement point is matched between computation and experiment for comparing surface pressure and skin friction data.

The boundary conditions are identified in Figure 1b. Inlet profiles for the computations are obtained from separate flat plate simulation at free-stream and wall boundary conditions identical to those listed above. The value of the momentum thickness reported in the experiments is matched to obtain the mean flow and turbulence profiles at the inlet boundary of the computational domain. The inlet profile for the mean flow variables are modified at the shock entry point to post-shock conditions calculated analytically. Post-shock conditions are also prescribed at the top boundary. At the wall, isothermal temperature of 300 K and no-slip boundary conditions are applied, and extrapolation condition is used at the exit boundary of the domain. For the turbulence quantities, the boundary conditions at the wall (Menter 1994) are taken as $k = 0$ and $\omega = 60\nu_w/\beta_1 \triangle y_1^2$, where ν_w is kinematic viscosity at the wall, $\beta_1 = 3/40$ and Δy_1 is the normal distance to the grid point nearest to the wall. Following Menter (1994), the freestream conditions used for the flat plate simulations are $\omega_\infty = 10\ U_\infty/L = 8.28 \times 10^3\ \mathrm{s}^{-1}$ and $k_\infty = 0.01\ \nu_\infty \omega_\infty = 1.87 \times 10^{-3}\ \mathrm{m}^2/\mathrm{s}^2$ where $L = 1$ m is a characteristic length of the plate. For the oblique shock wave/turbulent boundary layer interaction simulations, k and ω values at the boundary layer edge in the inlet profile are prescribed as the freestream conditions at the top boundary.

3.1. Grid convergence

A structured Cartesian mesh with exponential stretching normal to the wall is used to span the computational domain. Along the wall, the grid points are clustered at the origin and the mesh is stretched exponentially in the upstream and downstream directions. A careful grid refinement study is performed by systematically varying the number of grid points in each direction, as well as refining the cell size in critical regions. The skin friction coefficient is found to be most sensitive to the computational mesh and is used to identify a grid converged solution.

The grid refinement study for the $\beta = 14°$ strongest interaction is presented below. First, the distance of the first cell centre from the wall is successively halved from its initial value of 2×10^{-6} m. The corresponding values in wall units, y_2^+, are presented in Figure 2a. C_f plotted in Figure 2b indicate that 1×10^{-6} m is sufficient for an accurate solution. Next, the number of points in the wall parallel direction is refined until the two finest grids, 300 × 240 and 360 × 240, yield overlapping results in Figure 3. Finally, the number of points in the wall normal direction is increased to

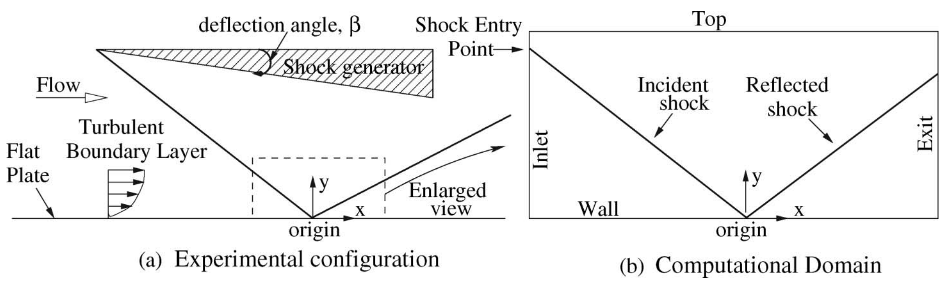

Figure 1. Oblique shock wave/turbulent boundary layer interaction on a flat plate: (a) experimental configuration with shock generator deflection angle β, (b) computational domain with appropriate boundary conditions.

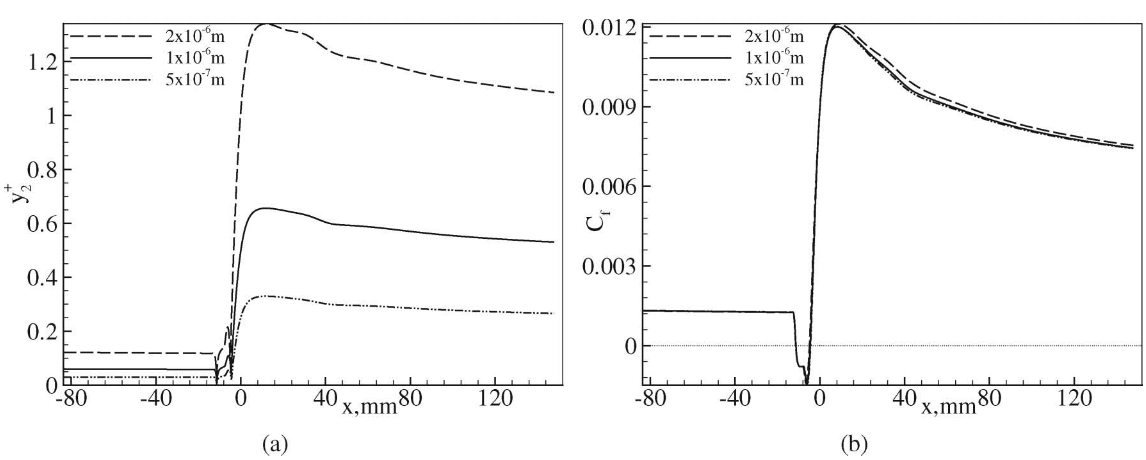

Figure 2. Variation in (a) y_2^+ at the wall and (b) skin friction coefficient for $\beta = 14°$ obtained using computational grids with varying wall normal spacing at the flat plate.

arrive at the 300 × 400 grid. Figure 4 shows that further refinement to 300 × 460 grid points yields less than 2% variation in wall pressure and skin friction. Based on the foregoing study, the solution obtained on the 300 × 400 grid is considered to be grid converged.

3.2. Shock-unsteadiness modification

The shock unsteadiness model was first proposed by Sinha *et al.* (2003) and was subsequently incorporated in one- and two-equation turbulence models (Sinha *et al.* 2005). The simplicity of the shock-unsteadiness correction term and its basis in underlying physical phenomena makes it attractive to use in practical applications. For easy reference, the highlights of the model and its implementation in the k–ω framework are presented below. Additional changes required for its application to the current oblique shock impingement problem are discussed in section 4.1.

In the k–ω model, the production of turbulent kinetic energy is given by:

$$P_k = \mu_{\mathrm{T}}\left(2S_{ij}S_{ji} - \frac{2}{3}S_{ii}^2\right) - \frac{2}{3}\bar{\rho}kS_{ii} \qquad (1)$$

where $S_{ij} = \frac{1}{2}(\partial\tilde{u}_i/\partial x_j + \partial\tilde{u}_j/\partial x_i)$ is the mean strain rate tensor and $\tilde{u}_i$ is the component of the Favre-averaged velocity in the x_i direction. The eddy viscosity is given by $\mu_{\mathrm{T}} = \bar{\rho}k/\omega$. In a shock wave, the production is proportional to S_{ii}^2, which is very large in magnitude. This results in excessively high values of k behind the shock.

Sinha *et al.* (2003) argue that the eddy viscosity assumption breaks down in the highly non-equilibrium

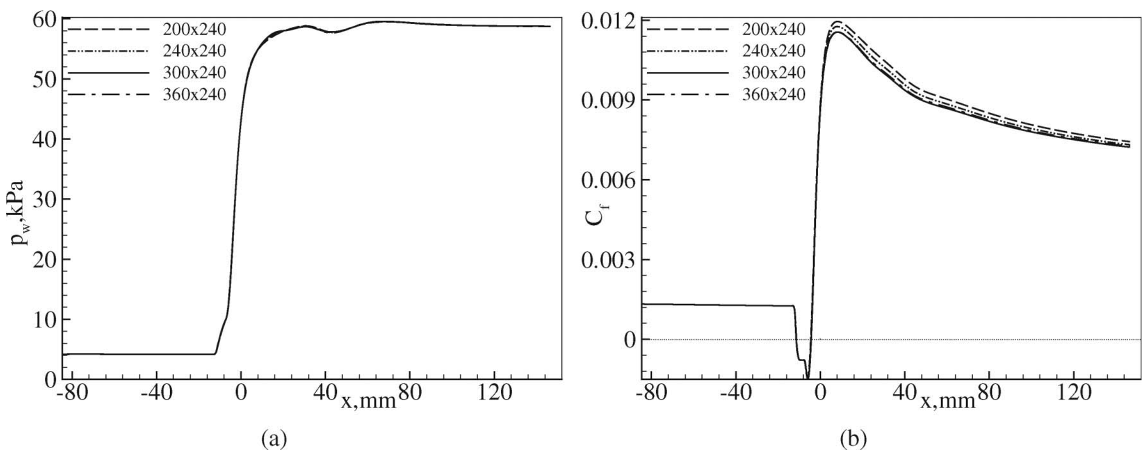

Figure 3. Variation in (a) wall pressure and (b) skin friction coefficient for $\beta = 14^\circ$ with changing number of wall-parallel grid points upstream of origin.

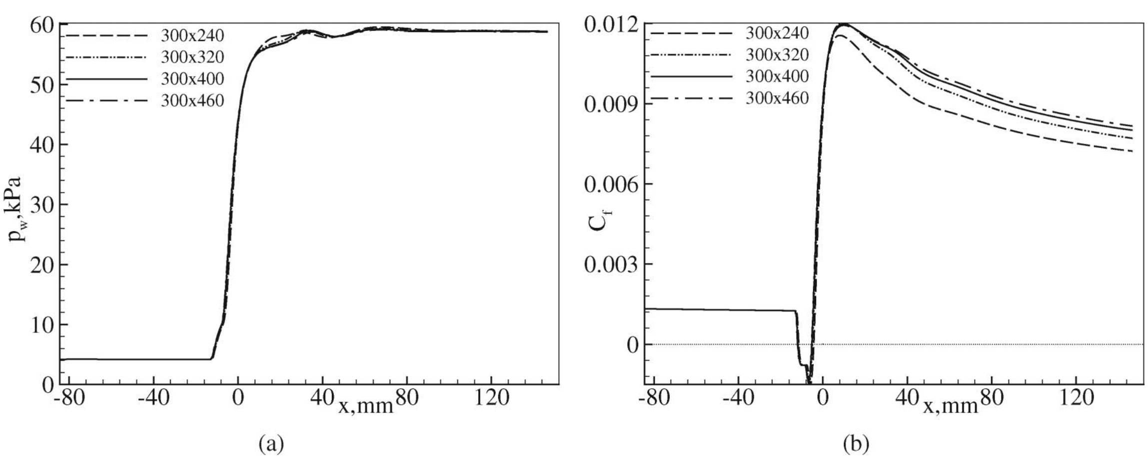

Figure 4. Effect of varying number of wall-normal grid points on computed (a) pressure and (b) skin friction coefficient for $\beta = 14^\circ$.

flow through a shock and a more accurate amplification of k is obtained by setting $\mu_T = 0$ in the production of turbulent kinetic energy. They also note that unsteady shock motion damps the amplification of k across a shock. Based on linear analysis results, they propose the following modification to the production term in a shock wave,

$$P_k = -\frac{2}{3}\bar{\rho}kS_{ii}(1 - b_1') \quad (2)$$

where

$$b_1' = \max[0,\ 0.4(1 - e^{1-M_{1n}})] \quad (3)$$

represents the damping effect caused by the coupling between the unsteady shock motion and the upstream velocity fluctuations. Here, M_{1n} is the shock-normal upstream Mach number measured in a frame of reference that is stationary with respect to the time-averaged shock wave. The above model is shown to accurately predict the amplification of k when homogeneous isotropic turbulence passes through a normal shock wave.

The shock-unsteadiness correction is applied in the k–ω framework by multiplying the eddy viscosity of the standard model by the factor,

$$c_\mu' = 1 - f_s\left[1 + \frac{b_1'}{\sqrt{3}\zeta}\right] \quad (4)$$

where $\zeta = S/\omega$ is dimensionless mean strain rate and the parameter $S = [2S_{ij}S_{ji} - (2/3)S_{ii}^2]^{1/2}$. The empirical function f_s locates the region of shock wave in terms of the ratio S_{ii}/S and was defined as (Sinha *et al.* 2005),

$$f_s = \frac{1}{2} - \frac{1}{2}\tanh[5(S_{ii}/S) + 3] \quad (5)$$

It takes a value of one in shock and high compression regions, such that $c_\mu' = -b_1'/\sqrt{3}\zeta$ and the modified production term in k–ω model matches with that in Equation (2). Otherwise, $f_s = 0$ and the standard form of k–ω model is recovered.

4. Results and discussions

The oblique shock wave/turbulent boundary layer interaction for 14° shock deflector is shown in Figure 5. The flow in the interaction region is complex due to the presence of multiple shock and expansion waves along with local flow separation and reattachment. A magnified view of the interaction region is shown in terms of the computed pressure and Mach number contours. The adverse pressure gradient of the incident shock separates the boundary layer on the flat plate. The streamline showing the extent of separation region is plotted and the separation and reattachment locations are identified by S and R, respectively. The separation shock and incident shock intersect and form induced and transmitted shock waves. The transmitted shock is short in length and terminates at the expansion waves generated by the flow turning over the separation bubble. The expansion fan is embedded between the induced and reflected shock waves. It interacts with and weakens the induced shock. It also causes the induced shock to bend and merge with the

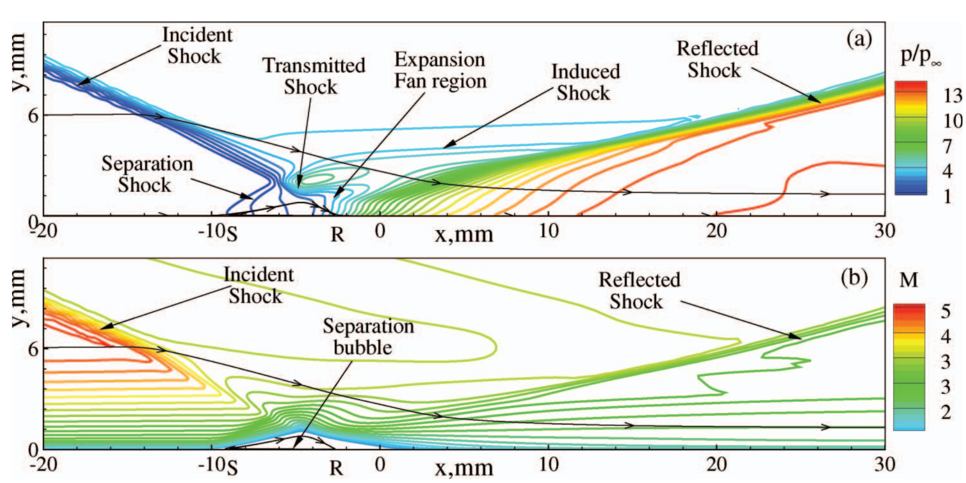

Figure 5. Computed (a) pressure and (b) Mach number contours showing different shocks, expansion waves and separation bubble for $\beta = 14°$ and $M_\infty = 5$. Standard k–ω model is used for the computation.

reflected shock. The compression waves generated by flow reattachment coalesce to form the reflected shock. The Mach number decreases from its freestream value of 5 ahead of the incident shock to about 3.6 at the induced shock and is further reduced to 2.7 by the reflected shock. In parallel, the flow is compressed through these shock waves with a decrease in the boundary layer thickness from its undisturbed value of 5.9 mm to 4 mm.

Figure 6 shows the variation in pressure and skin friction coefficient along the plate. The experimental pressure measurements remain at freestream value up to the separation point. It rises to about 16 kPa across the separation shock and rises further to about 58 kPa at flow reattachment. Adverse pressure gradient of the separation shock decreases the skin friction coefficient from its undisturbed boundary layer value. C_f is negative in the recirculation bubble and attains high values downstream of the interaction region.

The computations using the standard k–ω model show similar trends in surface pressure and skin friction coefficient variation. The major differences compared with the experimental data are in the size of the separation bubble and the skin friction at reattachment. The predicted separation point is far downstream of its experimentally measured location. The pressure rise at the separation shock is smaller, followed by a higher pressure gradient in the reattachment region. The computed results show some waviness in the pressure distribution downstream of reattachment. The experimental pressure data also show similar trend. This may be due to reflection of compression/expansion waves between the wall and the reflected shock. The zero crossing of the computed C_f determines the separation bubble size as 7.6 mm. The corresponding experimental value is 34 mm. The steep rise in skin friction at reattachment grossly overpredicts the measurements. C_f decreases further downstream to values closer to the experimental data. Similar results have been reported in literature (Lindblad, *et al.* 1998 Fedorova and Fedorchenko 2004, Gerolymos *et al.* 2004, Xiao *et al.* 2007). The shock-unsteadiness correction significantly improves the model predictions. The issues involved in the application of the modification and the results obtained are discussed in detail below.

4.1. *Application of shock-unsteadiness modification*

In order to incorporate shock-unsteadiness effects, we need to identify the shock waves and high compression regions in the flow. This is done by the function f_s. The correction term is to be applied at all grid points with non-zero f_s. The shock unsteadiness damping parameter b_1' is a function of M_{1n}. The shock-normal upstream Mach number M_{1n} is calculated by taking dot product of vector $\vec{u}_1/a_1$ with unit pressure gradient vector $\nabla p/|\nabla p|$.

$$M_{1n} = \frac{\vec{u}_1 \cdot \nabla p}{a_1|\nabla p|} \tag{6}$$

Here, $\vec{u}_1$ and a_1 are the velocity vector and speed of sound upstream of shock wave, respectively.

The shock waves and high compression regions in the standard k–ω solution are presented in terms of the mean dilatation S_{ii} in Figure 7. The quantity S_{ii} is normalised by the freestream velocity U_∞ and boundary layer thickness δ_0 upstream of the interaction region. S_{ii} becomes negative across the incident

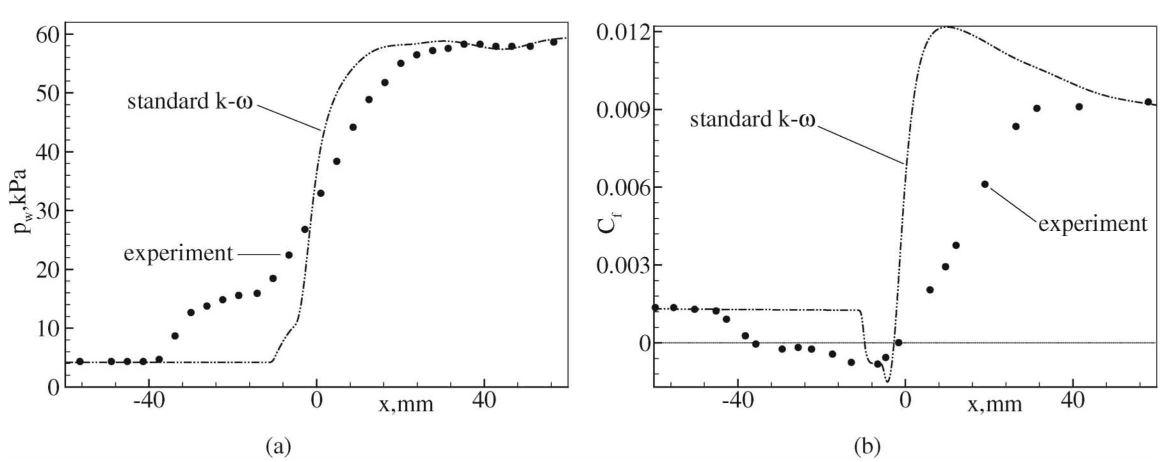

Figure 6. Variation in (a) wall pressure and (b) skin friction coefficient using standard k–ω model for $\beta = 14^\circ$ and $M_\infty = 5$. Experimental data of Schulein (2006) is presented for comparison (with permission of the American Institute of Aeronautics and Astronautics, Inc.).

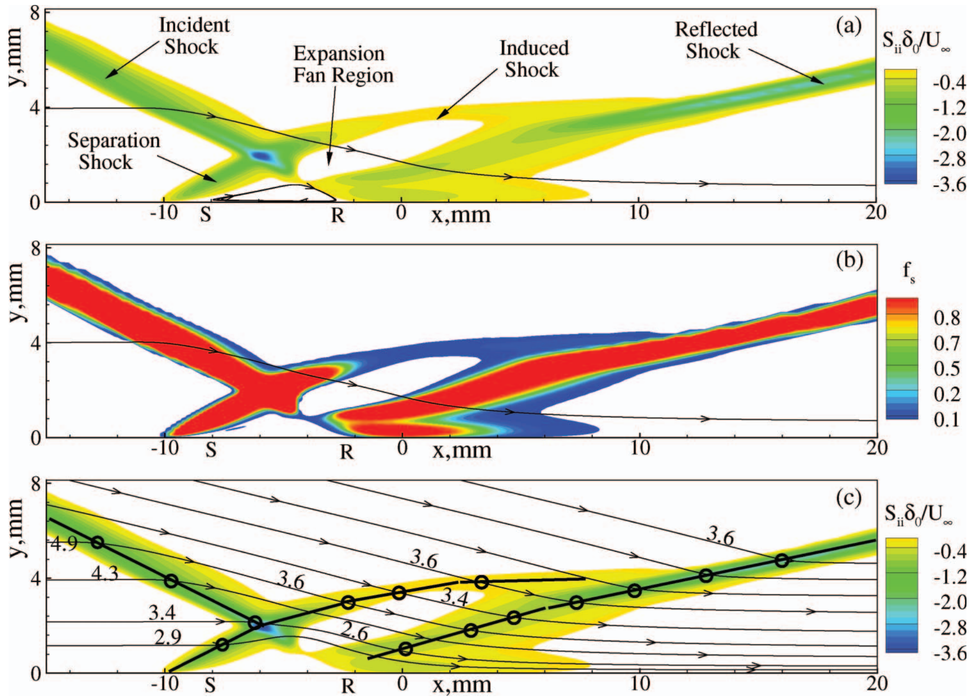

Figure 7. Distribution of (a) normalised mean dilatation and (b) f_s showing different shock regions in $\beta = 14^\circ$ interaction. (c) Points are identified in the shock waves and upstream Mach number is obtained along the corresponding streamlines.

and separation shocks and attains large negative values at the intersection of these two shock waves. S_{ii} also identifies the induced and transmitted shock waves. It is positive in the expansion fan. A large region of relatively low negative value of S_{ii} is observed in the reattachment region. This corresponds to the compression waves generated by gradual flow turning.

The original form of f_s proposed by Sinha *et al.* (2005) is a function of S_{ii}/S. This function when applied to the current configuration did not capture the separation shock well. This is because S attains high values in the lower part of the boundary layer and therefore reduces the magnitude of the ratio S_{ii}/S, such that $f_s < 0.65$. In an alternate form, S_{ii}/S is replaced by $S_{ii}\,\delta_0/V$, where V is the magnitude of the local velocity vector. This yields better reproduction of the separation shock. However, small velocities very close to the wall cause difficulties in numerical evaluation of f_s. Next, the maximum magnitude of mean dilatation $|S_{ii}|_{max}$ over the computational domain is used to normalise S_{ii} in the definition of f_s. Although this function identifies the shock well, it requires additional coding to identify the maximum value $|S_{ii}|_{\max}$, especially for parallel simulations run on multiple processors. Finally, the ratio of S_{ii} to U_∞/δ_0 is used to define a function of the form given below. The characteristic length δ_0 and velocity U_∞ are *a priori* known for a given simulation and can be specified as user input.

$$f_s = \frac{1}{2} - \frac{1}{2}\tanh[12(S_{ii}\delta_0/U_\infty) + 4] \qquad (7)$$

The constants chosen are such that f_s takes values close to one in strong shock regions and goes to zero outside shock waves. Depending on the level of compression, it smoothly varies between 0 and 1. Care is taken to make f_s negligible in boundary layer flows where the standard model predictions are well validated. Figure 7b shows the distribution of the above function in the interaction region and it captures the shock waves identified in Figure 7a correctly. Note that the definition of f_s is based on identifying the shock waves in the computational solution and no attempt has been made to tailor the function so as to match the pressure and skin friction measurements.

In the compression ramp flow (Sinha *et al.* 2005), the modification is active only in the separation shock. The flow upstream of the separation shock is well characterised and the variation of Mach number in the incoming boundary layer is readily available. By comparison, the regions of non-zero f_s in the current configuration correspond to the incident, separation, induced and reflected shock waves. Obtaining the local upstream Mach number at grid points at these shocks is much more challenging than the compression ramp case. Some of these values depend on the shock pattern in the intersection region and cannot be prescribed *a priori*. For example, for points in reattachment region upstream Mach number depends on the strength of the incident shock, induced shock and expansion waves.

The values of upstream Mach number at different shocks are calculated manually by identifying an upstream location along the local streamline in Figure 7c. For the separation shock upstream Mach number varies approximately from 1.1 to 3.4 and it increases from 3.4 to freestream value of 5 near the boundary layer edge for the incident shock. Downstream of the incident shock wave, Mach number decreases to around 3.6 for the induced shock. For the reflected shock wave, the upstream Mach number varies from around 2.0 near the reattachment point to 3.6 at the boundary layer edge. The average values of M_{1n} and b'_1 at the different shocks are listed in Table 1. As expected, b'_1 approaches zero in the near wall region and attains high values at the boundary layer edge. Incorporating the exact distribution of b'_1 in the code is a cumbersome task. A representative average value of 0.188 is used to apply the shock-unsteadiness modification, and sensitivity of the flow solution to variation of b'_1 is presented.

The main effect of the shock-unsteadiness modification is to reduce the amplification of turbulent kinetic energy across a shock wave. This effect can be seen in the normalised eddy viscosity contours plotted in Figure 8. Standard k–ω model results in a high level of eddy viscosity across incident shock and in the reattachment region. By comparison, the current shock-unsteadiness model yields much lower eddy viscosity levels in the interaction region. The computed eddy viscosity distribution using the original shock-unsteadiness modification of Sinha *et al.* (2005) is also shown in Figure 8b. This is very similar to the present model, except near the separation point, where μ_T/μ_∞ values are somewhat higher than that observed in Figure 8c.

Lower turbulence levels with the shock-unsteadiness model results in earlier separation and

Table 1. Average values of upstream Mach number normal to shock waves M_{1n} and shock unsteadiness damping factor b'_1.

Shock	M_1	M_{1n}	b'_1
Incident	3.4–5.0	1.89	0.23
Separation	1.1–3.4	1.28	0.09
Induced	3.4–3.6	1.61	0.18
Reflected	2.0–3.6	1.85	0.2

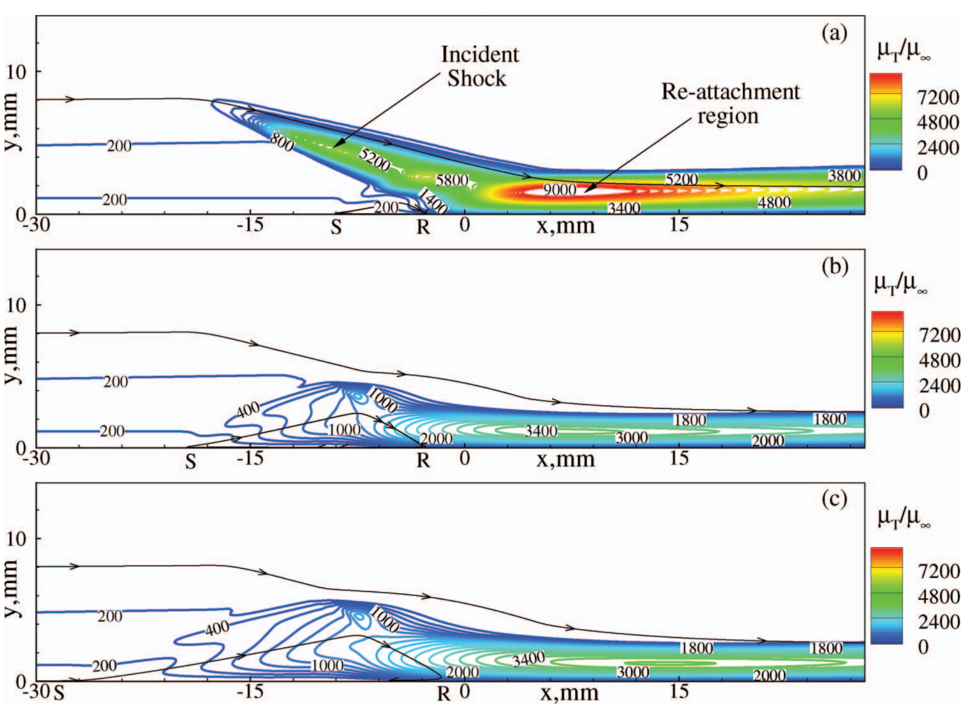

Figure 8. Normalised eddy viscosity contours obtained using (a) standard k–ω (b) original shock-unsteadiness (Sinha *et al.* 2005) and (c) present shock-unsteadiness models for $\beta = 14°$.

thus a larger separation bubble than standard *k–ω* model. The shock pattern obtained using shock unsteadiness modified *k–ω* model is shown in Figure 9 in terms of dilatation S_{ii} and pressure contours. It is qualitatively similar to that obtained using the standard *k–ω* model in Figure 5, but the location and shape of the different shock waves are altered by the shock-unsteadiness correction. Earlier separation using the modified *k–ω* model causes the separation shock to shift upstream closer to the experiment. It also increases the length of the separation and transmitted shocks. The transmitted shock is very small and is not clear in the standard *k–ω* solution. Larger size of the interaction region also leads to a more prominent expansion fan in Figure 9b than that obtained using the standard *k–ω* model.

The shock structure obtained using the current shock-unsteadiness correction has striking resemblance to the experimental shadowgraph (Schulein 2006) presented in Figure 9c. The high compression – negative S_{ii} – regions match the corresponding dark lines in experimental shadowgraph. These include the incident, separation, induced and transmitted shocks as well as the curved pattern of the reflected shock. The experimental shadowgraph is explained in the flow diagram in Figure 9c. The expansion fan generated over the separation bubble curves the induced shock downwards. The reflected shock on the other hand is curved upwards by the expansion fan. The pressure contours in Figure 9b clearly show the interaction of the expansion fan with the shock waves. The only difference between experiment and computation being the upward curving of the induced and reflected shocks caused by a second expansion fan emanating from the end of the shock generator. This effect and the resulting delay in the intersection of the two shocks is not reproduced in the computed solution. This is because the shock generator geometry is not included in the current simulations.

Wall pressure and skin friction coefficient computed using the shock unsteadiness modified *k–ω* model are compared with the experiment and standard *k–ω* model in Figure 10. The shock-unsteadiness modification appreciably improves the flow predictions in the interaction region. The location of the separation shock pressure rise is much closer to the experiment than the standard model. This results in a better comparison of the pressure plateau as well as the pressure rise in the reattachment region with the measurements. A similar trend is observed in the skin-friction results with the drop in C_f at separation point being closer to the experimental data. The reattachment point is not affected much by the modification and both model predictions compare well with experiment. Past reattachment point, the shock-unsteadiness modified *k–ω* model reproduces the initial build-up of C_f well, but

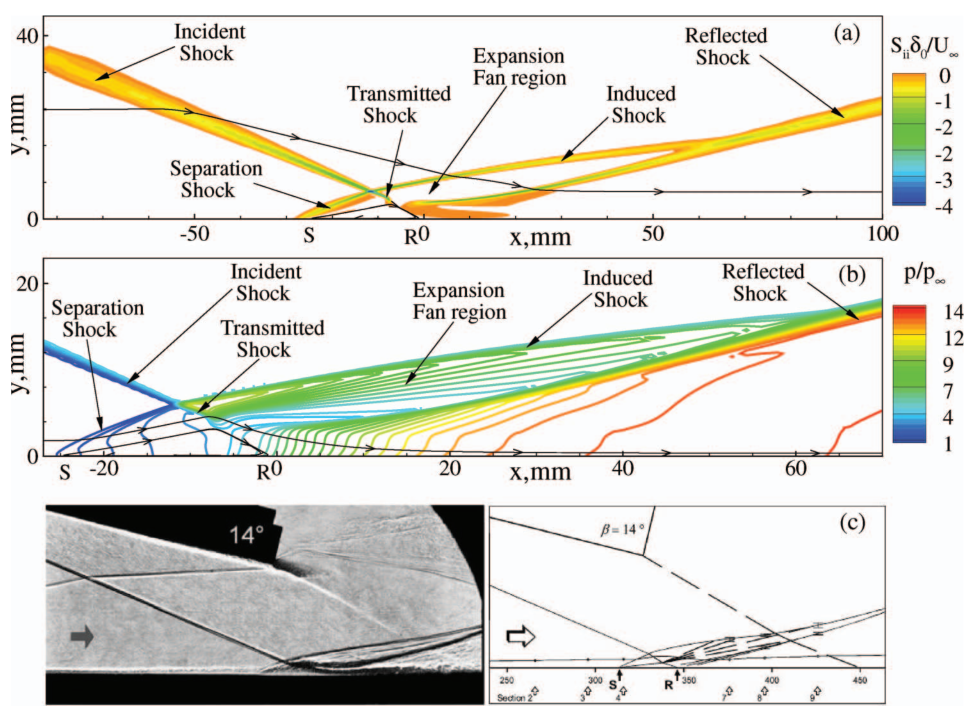

Figure 9. Computations showing (a) normalised mean dilatation and (b) pressure contours using shock unsteadiness modified *k–ω* model for $\beta = 14^\circ$, compared with (c) experimental shadowgraph and schematic (Schulein 2006), with permission of the American Institute of Aeronautics and Astronautics, Inc.

saturates at a value lower than the experimental data. By comparison, the standard k–ω model predicts a steep rise in C_f at reattachment followed by a gradual decrease. The maximum C_f predicted at $x = 10$ mm is significantly higher than the measurement.

The close match of experimental skin friction value and standard k–ω prediction at $x \sim 50$ mm is fortuitous. Computation over a larger domain extending up to $x = 500$ mm (Figure 11) shows that the standard k–ω results eventually asymptote to a value close to the modified k–ω model prediction. The small difference between the two asymptotic C_f values is caused by a build-up of eddy viscosity outside the boundary layer in the standard k–ω solution. Figure 12 shows the eddy viscosity distribution downstream of the interaction region. The standard k–ω model yields very high turbulence amplification across the reflected shock, with μ_T/μ_∞ levels in the post-shock inviscid flow exceeding its value in the boundary layer. Profiles of eddy viscosity plotted at different stream-wise locations downstream of reattachment point (Figure 13) show this effect more clearly. High values of μ_T/μ_∞ at the boundary layer edge distort the eddy viscosity distribution in the boundary layer, and this non-physical effect persists far downstream of the interaction region. By comparison, the eddy viscosity distribution in the modified k–ω solution resembles that of a unperturbed zero pressure gradient turbulent boundary layer for $x > 150$ mm.

The location of separation and reattachment points computed using the standard k–ω and current shock-unsteadiness modified k–ω models is listed in Table 2. The corresponding points from oil flow visualisation in the experiment are also tabulated.

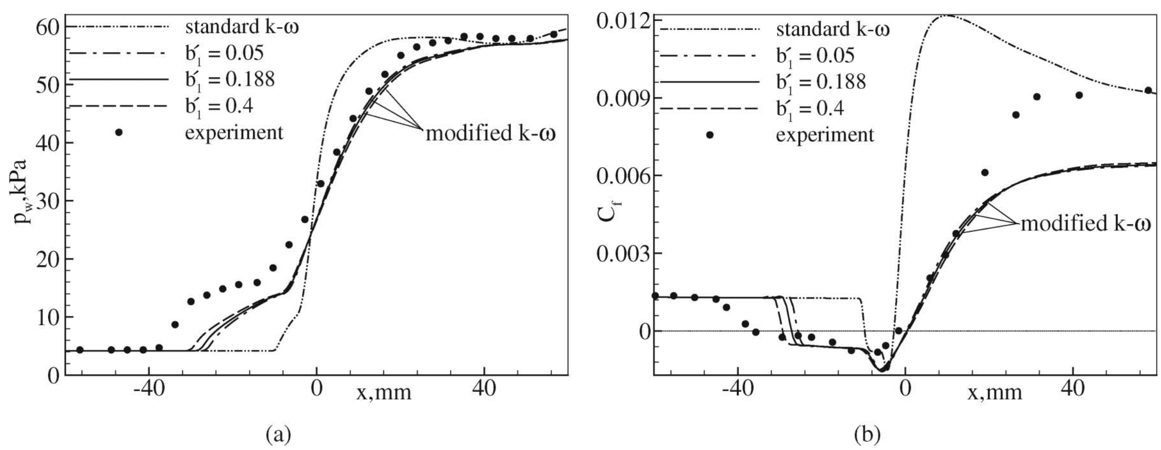

Figure 10. Computed (a) wall pressure and (b) skin friction coefficient for $\beta = 14^\circ$ using standard k–ω and shock-unsteadiness modified k–ω models with different values of b'_1, compared with experiments.

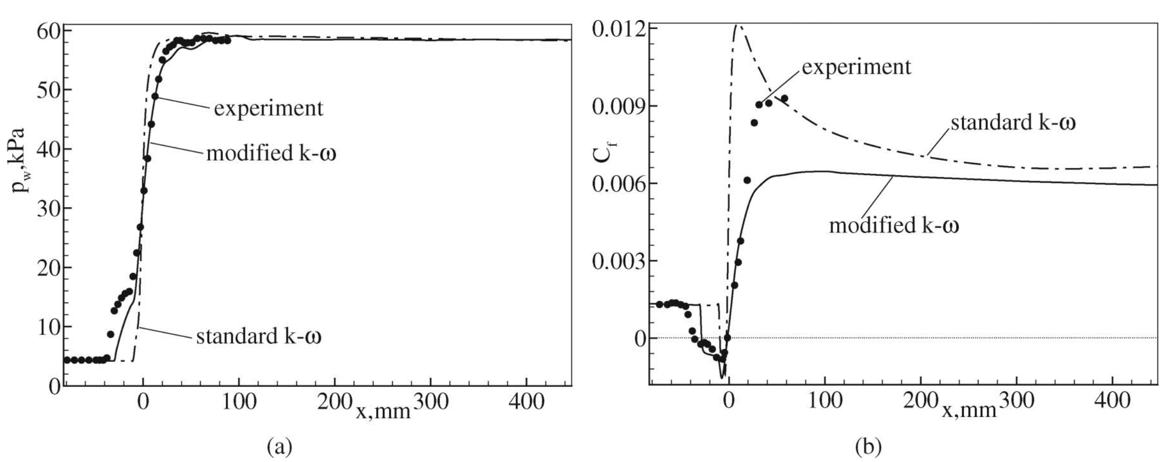

Figure 11. Comparison of (a) wall pressure and (b) skin friction coefficient for $\beta = 14^\circ$ computed using standard k–ω and shock-unsteadiness modified k–ω models over a larger domain up to 500 mm downstream of interaction region. Experimental data (Schulein 2006) is reproduced with the permission of the American Institute of Aeronautics and Astronautics, Inc.

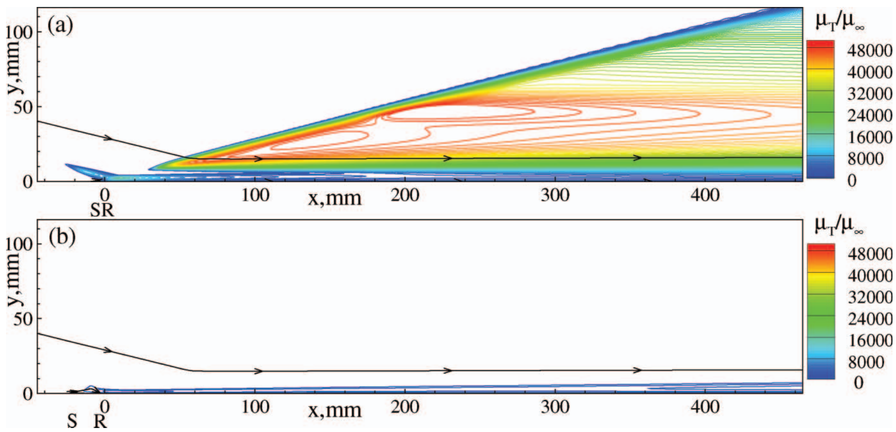

Figure 12. Normalised eddy viscosity contours obtained using (a) standard k–ω and (b) shock-unsteadiness modified k–ω models downstream of reattachment for $\beta = 14^\circ$.

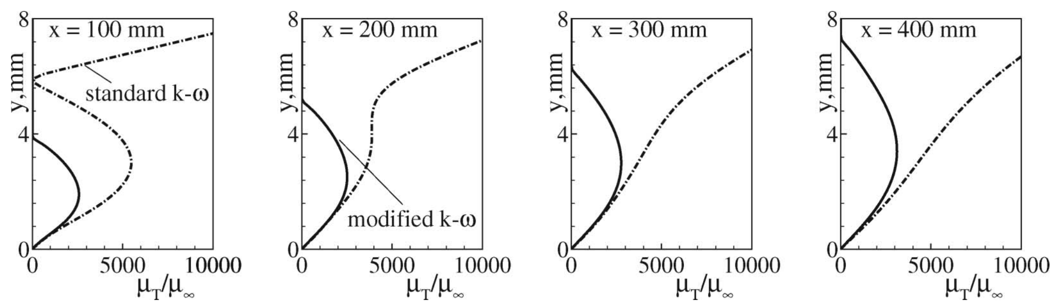

Figure 13. Normalised eddy viscosity profiles at different stream-wise stations downstream of interaction region computed using standard k–ω and shock-unsteadiness modified k–ω models for $\beta = 14^\circ$.

Table 2. Comparison of computed separation and reattachment points and separation bubble size with experiments.

	Separation point[a] (mm)			Reattachment point[b] (mm)			Separation bubble size (mm)		
(β°)	Experiment	Standard k–ω	Modified k–ω	Experiment	Standard k–ω	Modified k–ω	Experiment	Standard k–ω	Modified k–ω
14	35.7	9.9	27.1	1.7	2.3	−0.4	34	7.6	27.5
10	16.2	6.9	13.5	4.2	3.5	2.6	12	3.4	10.9
6	–	5.7	7.8	–	4.7	3.9	–	1.0	3.9

[a,b] All distances are measured from origin in upstream direction.

Quantitative comparison shows that the shock-unsteadiness correction markedly improves separation location. As a result, the separation bubble size is increased from 22 to 81% of the experimental measurement.

The sensitivity of pressure and skin friction prediction to the choice of shock-unsteadiness model parameter b_1' is also presented in Figure 10. The value of b_1' is varied from lowest to highest attainable values of 0.05 to 0.4. There is negligible effect of b_1' variation on the surface properties except for the location of the separation shock. A higher b_1' enhances the damping of turbulent kinetic energy, resulting in lower turbulence at the shock and thereby earlier separation. However, the variation in separation location is within 7% of that obtained using the average value of b_1'.

4.2. $\beta = 10^\circ$ and 6° cases

Shock generator angles of 10° and 6° are simulated using the standard and modified k–ω models and results are compared with experimental shadowgraphs and surface measurements. A 240 × 400 computational grid is used in these simulations, which is based on a grid refinement study similar to the 14° case. Details are omitted for the sake of brevity. The shock-unsteadiness correction is implemented in these flows using the same values of b_1' and f_s as discussed earlier.

The shadowgraphs in Figures 14 and 15 show a reduction in the intensity of the interaction than the 14° case, in terms of smaller separation bubble size. The pressure and skin friction data in Figure 16 reflect the same trend with the values of separation and reattachment points listed in Table 2. As in the case of 14° shock generator, the standard k–ω model underpredicts the separation bubble size and overpredicts the skin friction coefficient at reattachment. The shock-unsteadiness modification moves the separation location closer to experiment for $\beta = 10°$ and increases the bubble size from 28 to 91% of the experimental value. For the 6° case a separation bubble was not identified in the oil flow pattern. The standard model predicts an incipient separation in this flow as in Figure 17 and the modification increases the size of the bubble by a small amount. Pressure and C_f measurements for this case are not available.

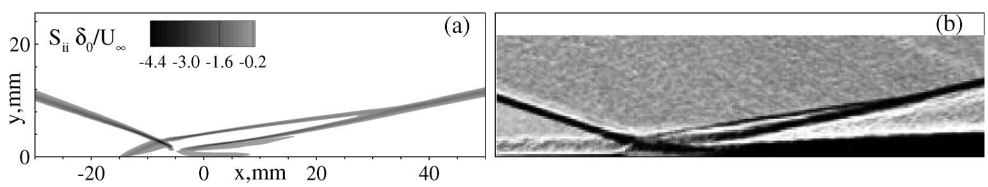

Figure 14. (a) Normalised mean dilatation contours computed using shock unsteadiness modified k–ω model for $\beta = 10°$ and $M_\infty = 5$, compared with (b) experimental shadowgraph (Schulein 2006), with permission of the American Institute of Aeronautics and Astronautics, Inc.

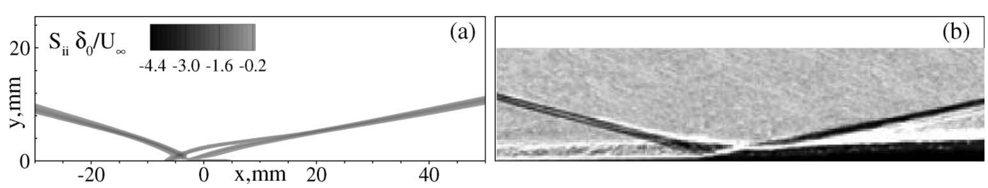

Figure 15. (a) Normalised mean dilatation contours computed using shock unsteadiness modified k–ω model for $\beta = 6°$ and $M_\infty = 5$, compared with (b) experimental shadowgraph (Schulein 2006), with permission of the American Institute of Aeronautics and Astronautics, Inc.

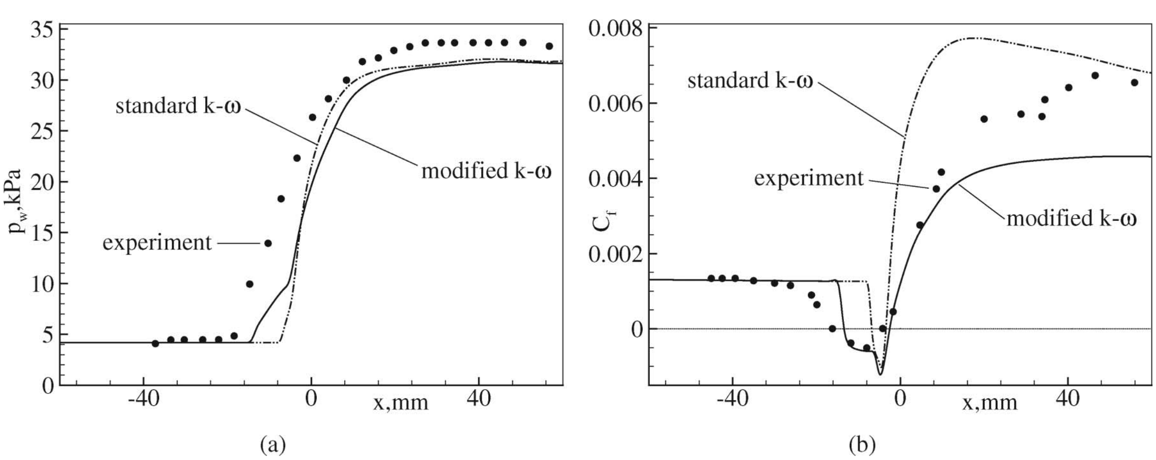

Figure 16. Computed (a) wall pressure and (b) skin friction coefficient for $\beta = 10°$ at $M_\infty = 5$ using standard k–ω and shock-unsteadiness modified k–ω models, compared with experiments (Schulein 2006), with permission of the American Institute of Aeronautics and Astronautics, Inc.

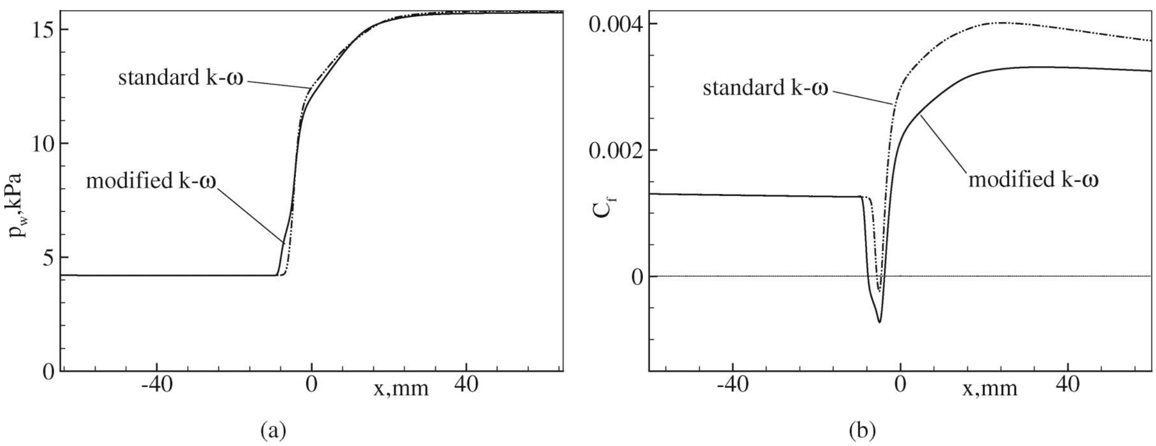

Figure 17. Computed (a) wall pressure and (b) skin friction coefficient for $\beta = 6^\circ$ at $M_\infty = 5$ using standard k–ω and shock-unsteadiness modified k–ω models.

5. Conclusions

In this article, we study the impingement and reflection of an oblique shock wave on a turbulent boundary layer. Three configurations with shock generator angles of 14, 10 and 6° are chosen at Mach 5. Both standard k–ω model and shock-unsteadiness modified k–ω models are applied, and results are compared with experimental data.

In spite of the geometric simplicity, presence of multiple shock waves and flow expansion in the interaction region makes it challenging to implement the shock-unsteadiness correction. Several forms of the shock identifier function f_s are tested to arrive at its final form. The value of upstream Mach number, required for calculating the correction term cannot be prescribed *a priori*. However, careful study shows that the results are not sensitive to variation of the upstream Mach number, as long as the shock regions are identified correctly.

The standard k–ω model predicts delayed flow separation and yields too high skin friction at reattachment. The damping effect of the shock-unsteadiness correction moves the separation location much closer to the experiment. This in turn results in close matching of the shock structure with the experimental shadowgraph. Comparison with surface measurements show that the shock-unsteadiness modification yields appreciable improvement over the standard k–ω model, especially near the separation point and in the reattachment region. It however underpredicts the skin friction coefficient in the recovering boundary layer downstream of the interaction.

For varying shock generator angles, the shock-unsteadiness modified k–ω model reproduces the correct physical trend of reduced separation bubble size with decreasing shock strength. Also, the effect of the correction term, or equivalently the difference between the standard and modified models, diminishes for weaker interaction for which standard models yield a reasonably accurate result.

Acknowledgement

The authors thank Indian Space Research Organisation (ISRO) for supporting this research under the RESPOND programme.

References

Coakley, T.J. and Huang, P.G., 1992. Turbulence modeling for high speed flows. *AIAA Paper*, AIAA-92-0436.

Fedorova, N.N. and Fedorchenko, I.A., 2004. Computations of interaction of incident oblique shock wave with a turbulent boundary layer on a flat plate. *Journal of Applied Mechanics and Technical Physics*, 45 (3), 358–366.

Gerolymos, G.A., Sauret, E., and Vallet, I., 2004. Oblique shock wave/boundary layer interaction using near-wall Reynolds stress models. *AIAA Journal*, 42 (6), 1089–1100.

Lindblad, I.A.A., *et al.*, 1998. A prediction method for high speed turbulent separated flows with experimental verification. *AIAA Paper*, AIAA-98-2547.

MacCormack, R.W. and Candler, G.V., 1989. The solution of Navier–Stokes equations using Gauss-Siedal line relaxation. *Computers and Fluids*, 17 (1), 135–150.

Menter, F.R., 1994. Two-equation Eddy-viscosity turbulence models for engineering applications. *AIAA Journal*, 32 (8), 1598–1605.

Schulein, E., 2006. Optical skin friction measurements in short-duration facilities. *AIAA Journal*, 44 (8), 1732–1742.

Sinha, K., Mahesh, K., and Candler, G.V., 2005. Modeling the effect of shock-unsteadiness in shock/turbulent boundary layer interactions. *AIAA Journal*, 43 (3), 586–594.

Sinha, K., Mahesh, K., and Candler, G.V., 2003. Modeling shock-unsteadiness in shock/turbulence interaction. *Physics of Fluids*, 15 (8), 2290–2297.

Sinha, K. and Candler, G.V., 1998. Convergence improvement of two-equation turbulence model calculations. *AIAA Paper*, AIAA-98-2649.

Viegas, J.R. and Horstman, C.C., 1979. Comparison of multi-equation turbulence models for several shock boundary interaction flows. *AIAA Journal*, 17 (8), 811–820.

Wilcox, D.C., 1988. Reassessment of the scale-determining equation for advanced turbulence models. *AIAA Journal*, 26 (11), 1299–1310.

Wilcox, D.C., 1998. *Turbulence modeling for CFD*. 2nd ed. La Canada, CA: DCW Industries.

Wright, M.J., Candler, G.V., and Bose, D., 1998. Data-parallel line relaxation method for the Navier–Stokes equations. *AIAA Journal*, 36 (9), 1603–1609.

Xiao, X., *et al*., 2007. Role of turbulent prandtl numbers on heat flux at hypersonic Mach numbers. *AIAA Journal*, 45 (4), 806–813.